

# THE PALE GREEN DOT: A METHOD TO CHARACTERIZE PROXIMA CENTAURI b USING EXO-AURORAE

RODRIGO LUGER<sup>1,3,4,5</sup>, JACOB LUSTIG-YAEGER<sup>1,3,4</sup>, DAVID P. FLEMING<sup>1,3</sup>, MATT A. TILLEY<sup>2,3,4</sup>, ERIC AGOL<sup>1,3,4</sup>, VICTORIA S. MEADOWS<sup>1,3,4</sup>, RUSSELL DEITRICK<sup>1,3,4</sup>, AND RORY BARNES<sup>1,3,4</sup>

*Draft version May 27, 2022*

## ABSTRACT

We examine the feasibility of detecting auroral emission from the potentially habitable exoplanet Proxima Centauri b. This planet’s active, late-type M dwarf host makes detection of aurorae more favorable than around a solar-type star, primarily by increasing auroral power and improving the planet-star contrast in the visible wavelength range due to strong TiO absorption in the star. Detection of aurorae would yield an independent confirmation of the planet’s existence, constrain the presence and composition of its atmosphere, and determine the planet’s eccentricity and inclination, thereby breaking the mass-inclination degeneracy. If Proxima b is a terrestrial world with an atmosphere and magnetic field, we estimate that its auroral power at the 5577Å OI auroral line is on the order of 0.1 TW under steady-state stellar wind, or  $\sim 100\times$  stronger than that on Earth. This corresponds to a planet-star contrast ratio of  $10^{-6} - 10^{-7}$  in a narrow band about the 5577Å line, although higher contrast ( $10^{-4} - 10^{-5}$ ) may be possible during periods of strong magnetospheric disturbance (auroral power 1 – 10 TW). We searched the high spectral resolution Proxima b HARPS data for the 5577Å line and for other prominent oxygen and nitrogen lines, but find no signal, indicating that the OI auroral line contrast must be lower than  $2 \times 10^{-2}$  (with power  $\lesssim 3,000$  TW), consistent with our predictions. We find that observations of 0.1 TW auroral emission lines are likely infeasible with current and planned telescopes. However, future observations with a large-aperture, space-based coronagraphic telescope or a ground-based extremely large telescope (ELT) with a coronagraph could push sensitivity down to terawatt oxygen aurorae (contrast  $7 \times 10^{-6}$ ) with exposure times of  $\sim 1$  day at high spectral resolution. If a coronagraph design contrast of  $10^{-7}$  can be achieved with negligible instrumental noise, a future concept ELT could observe steady-state auroral emission in a few nights.

*Subject headings:* planets and satellites: terrestrial planets, atmospheres, aurorae, detection — Proxima Centauri b

## 1. INTRODUCTION

The discovery of Proxima Centauri b (henceforth ‘Proxima b’), only 1.3pc distant from the Sun (Anglada-Escudé et al. 2016), ushers in a new era of characterization of nearby potentially habitable exoplanets. Although Proxima b is not known to transit—making transmission spectroscopy impossible—it is an ideal candidate for high-contrast direct spectroscopy using an extremely large coronagraph-equipped telescope. However, even with the enhancement in angular resolution provided by the proximity of its host star, Proxima b’s close-in orbit ( $a = 0.0485$  AU; Anglada-Escudé et al. 2016) precludes imaging with current coronagraphs, such as the Gemini Planet Imager (GPI; Macintosh et al. 2014) and the Very Large Telescope’s Spectro-Polarimetric High-contrast Exoplanet REsearch facility (VLT-SPHERE; Beuzit et al. 2008), which operate primarily in the near-infrared. This is in part due to the poorer Strehl ratios currently achievable at visible wavelengths with ground-

based adaptive optics (AO) systems<sup>6</sup>. Consequently, in advance of larger diameter ground- and space-based telescopes, and improvements in visible AO systems, we must initially consider observations that do not rely on transits or current coronagraphy to search for and characterize the atmosphere of Proxima b.

Phase curves may offer one of the first means to study the atmosphere of Proxima b (Turbet et al. 2016; Kreidberg & Loeb 2016; Meadows et al. 2016) by potentially showing the reduction in day-night thermal emission contrast associated with an atmosphere. Phase curves have proven to be a successful means to characterize the atmospheres of planets larger and hotter than Proxima b (Cowan et al. 2007; Knutson et al. 2007; Knutson et al. 2008; Crossfield et al. 2010; Brogi et al. 2012; Zellem et al. 2014; Stevenson et al. 2014), including ones that do not transit (Selsis et al. 2011; Faigler & Mazeh 2011; Maurin et al. 2012; Brogi et al. 2014). However, the expected planet-star contrast ratio in the visible and NIR due to reflected stellar radiation is likely to be below the anticipated systematic noise floor for JWST/NIRSpec (Meadows et al. 2016), and although the planet-star contrast ratio becomes quite favorable beyond  $10\mu\text{m}$ , where the planetary thermal emission peaks, mid-IR phase curves will require JWST/MIRI.

<sup>1</sup> Astronomy Department, University of Washington, Box 951580, Seattle, WA 98195

<sup>2</sup> Department of Earth & Space Sciences, University of Washington, Box 351310, Seattle, WA 98195

<sup>3</sup> NASA Astrobiology Institute – Virtual Planetary Laboratory Lead Team, USA

<sup>4</sup> Astrobiology Program, University of Washington, 3910 15th Ave. NE, Box 351580, Seattle, WA 98195, USA

<sup>5</sup> rodluger@uw.edu

<sup>6</sup> See, e.g., <https://www.eso.org/sci/facilities/paranal/instruments/sphere/overview.html>

To complement the anticipated JWST thermal phase curve measurements, in this work we explore the possibility of directly detecting optical auroral emission from the atmosphere of Proxima b using high-resolution optical spectroscopy. Numerous studies have investigated exoplanet aurorae in the radio due to cyclotron and synchrotron emission to constrain the planetary magnetic field (e.g. Bastian et al. 2000; Grießmeier et al. 2007; Zarka 2007; Hess & Zarka 2011; Driscoll & Olson 2011). Smith et al. (2004) modeled the role of aurorae in redistributing high energy incident stellar flux to the surface of terrestrial exoplanets, and Rimmer et al. (2015) considered the effect of aurorae on the optical and infrared spectra of gaseous exoplanets. Sparks & Ford (2002) suggested that exoplanet airglow and/or aurorae could be detected with a combination of high contrast imaging and high dispersion spectroscopy. However, a detailed calculation of the expected auroral signal strength on a nearby exoplanet and the feasibility of its detection has not yet been fully performed.

Detecting optical auroral emission from the possible atmosphere of Proxima b is likely much more favorable for this system than for an Earth-Sun analog. This is due to both planetary and stellar characteristics that favor auroral production and improve detectability. In particular, Proxima b’s intrinsic planetary properties may favor production of aurorae from O atoms. If Proxima b is Earth-like in composition, recent dynamical/planetary interior modeling results by Barnes et al. (2016) and Zuluaga & Bustamante (2016) suggest that the planet may have a magnetic field, potentially increasing the likelihood of atmospheric retention and of auroral emission. Atmospheres rich in oxygen-bearing molecules, including O<sub>2</sub> and CO<sub>2</sub>, have been predicted for Proxima b (Meadows et al. 2016) as a result of the evolutionary processes for terrestrial planets orbiting M dwarfs (Luger & Barnes 2015; Barnes et al. 2016). On Earth, the oxygen (OI) auroral line at 5577Å provides the distinctive green glow observed in both the Aurora Borealis and the Aurora Australis, and is the brightest auroral feature (Chamberlain 1961; Dempsey et al. 2005). For emissions from the upper atmosphere, only the 1.27μm O<sub>2</sub> airglow and combined near-infrared OH nightglow features are brighter (Hunten et al. 1967). The oxygen green line is seen in both the Earth’s O<sub>2</sub>-rich atmosphere (Chamberlain 1961) and Venus’ CO<sub>2</sub>-dominated atmosphere (Slanger et al. 2001), where it has been observed to increase in brightness after CME events (Gray et al. 2014).

The stellar properties and the planet-star separation are also likely to enhance the auroral power on Proxima b relative to an Earth-Sun analog. Proxima Centauri is an active flare star with a magnetic field ~600× stronger than that of the Sun (Reiners & Basri 2008; Davenport et al. 2016). Since stellar activity drives auroral emission for an Earth-like magnetosphere, such features may be much stronger on planets orbiting active M dwarfs. Additionally, with a close-in orbit of 0.0485 AU, Proxima b is about 20× closer to Proxima Centauri than the Earth is to the Sun (Anglada-Escudé et al. 2016). This proximity further increases particle fluxes incident on the planetary atmosphere that drive ionization and the subsequent recombination radiation.

In addition to increasing the likelihood and strength

of the aurora, the characteristics of the Proxima Centauri system may also enhance its detectability. Since the Proxima system is only 1.3pc away, it is perhaps the best-case scenario for the detection of the faint auroral signal from a terrestrial exoplanet. Even though the planet-star contrast ratio in reflected visible light is poor ( $\lesssim 10^{-7}$ ; see Turbet et al. 2016; Kreidberg & Loeb 2016; Meadows et al. 2016), if Proxima b exhibits auroral emission, this will brighten the planet and potentially boost the planet-star contrast by one or more orders of magnitude at the wavelengths of the auroral emission features. The short wavelength of the oxygen green line also improves the contrast of the planet relative to the star due to the star’s cool temperature and TiO absorption, which strongly suppresses the brightness of the star in the visible. This improvement in contrast is significantly less for the near-infrared O<sub>2</sub> 1.27μm and OH airglow lines. In addition to increasing the contrast, the small semi-major axis of Proxima b results in an orbital velocity of ~50 km/s, which will cause its auroral emission to be Doppler-shifted by as much as 1Å over the course of its orbit, making it easier to disentangle it from stellar features via high resolution spectroscopy. An additional advantage of the short wavelength of the OI feature is the smaller inner working angle and point-spread function that may be achieved with a coronagraph at that wavelength (Agol 2007). These factors all improve the chance of detection with ground-based telescopes.

The detection of the oxygen auroral line at 5577Å would provide an important diagnostic for planetary properties. Its detection would not only confirm the presence of the planet, but would point to the presence of an atmosphere with abundant oxygen atoms, which is more likely to indicate a terrestrial body. Additionally, the detection of the line would yield a measurement of the radial velocity (RV) of the planet, which combined with the RV measurements of the star (Anglada-Escudé et al. 2016) would enable the measurement of the eccentricity and inclination of the orbit, ultimately yielding the mass of the planet. Detection of the oxygen auroral line would therefore provide several key planetary parameters that could be used to constrain Proxima b’s potential habitability (Barnes et al. 2016; Meadows et al. 2016).

This paper is organized as follows: in §2 we calculate the expected auroral emission strength of Proxima b under different assumptions of stellar and planetary properties. In §3 we model the planet-star contrast ratio in a narrow band centered on the OI 5577Å line and calculate the integration times required to detect the feature with different instruments. In §4 we conduct a preliminary search for auroral emission in the HARPS high-resolution, ground-based spectroscopy used by Anglada-Escudé et al. (2016) for the RV detection of Proxima b. Finally, in §5 we discuss our results and present our conclusions.

## 2. AURORAL SIGNAL STRENGTH

Below, we quantitatively estimate the auroral intensity for steady-state stellar input. We employ two different methods to compare and contrast the regimes for both an Earth-like and a Neptune-like planetary magnetic dipole moment and anticipated auroral production efficiency. Both planets are assumed to be terrestrial bodies with

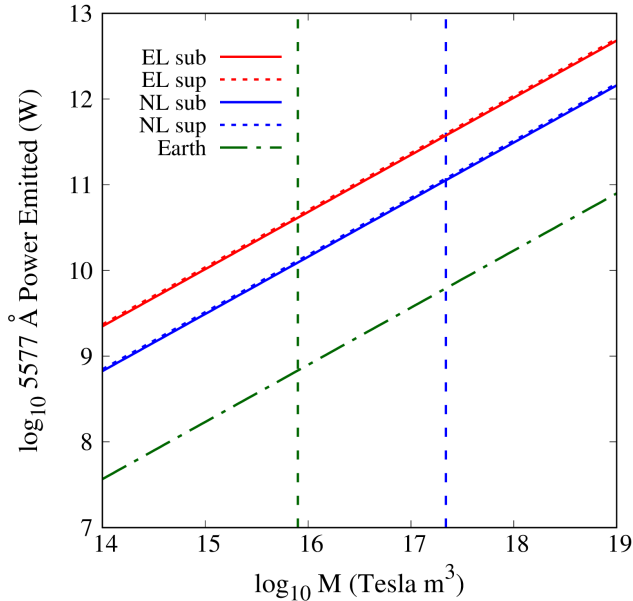


FIG. 1.— Predicted 5577Å auroral power as a function of planetary magnetic dipole moment calculated using the stellar wind scaling method from §2.2. Solid (dotted) lines correspond to the sub-(super-) Alfvénic stellar wind conditions; red (blue) lines correspond to an Earth-like (Neptune-like) planetary magnetic dipole with conversion efficiency of  $\sim 1\%$  ( $\sim 0.3\%$ ) for Proxima b. The green dash-dotted line corresponds to Earth in its natural orbit around the Sun. The dashed vertical green (blue) line indicates the magnitude of Earth’s (Neptune’s) magnetic dipole moment.

the orbital characteristics of Proxima b. Method 1 involves a simple estimation of the emitted electromagnetic auroral power driven by the stellar wind power delivered at the magnetopause of the planet. Method 2 uses the prediction of a magnetohydrodynamical (MHD) model that was empirically tuned to calculate the auroral response at Earth, with modifications to the relevant inputs of the stellar wind of Proxima Centauri and assumed planetary parameters for Proxima b (Anglada-Escudé et al. 2016).

The quantities we calculate include only the estimated, localized emissions caused by magnetospheric particle precipitation into a discrete auroral oval — not the diffuse, global phenomenon of airglow. On Earth, the 5577Å airglow can be visible to the naked eye and could be significant on Proxima b, but is driven by different physical processes (e.g., nighttime recombination due to dayside photoionization) that are outside the scope of this analysis. Similarly, the 5577Å airglow has been observed at Venus (e.g. Slanger et al. 2001) and Mars (e.g. Seth et al. 2002) — both having no present-day global magnetic field. For these reasons we cannot suggest basing the existence of or placing constraints on Proxima b’s planetary magnetic field based on the detection of this auroral line.

### 2.1. Stellar winds at Proxima b

M dwarf mass-loss rates, and therefore stellar winds, are not well constrained due to observational sparsity and difficulty (e.g. Wood et al. 2004). To model the M dwarf winds for Proxima Centauri, we adopt the predictions

from the modeling efforts of Cohen et al. (2014), who generated an MHD stellar wind model for the M3.5 star EV Lacertae based on available observations. There are two primary differences between EV Lac and Proxima Centauri that we should take into account when considering the stellar wind at our planet’s location of interest: 1) the relative mass-loss rates, 2) the difference in rotation rates.

The first of these factors has been estimated by Wood et al. (2005), who find that the mass-loss per unit surface area for Proxima Centauri and EV Lacertae as quite similar. This suggests comparable wind conditions at equal distances in units of their respective stellar radii.

The second factor, the rotation rate, affects the morphology of the stellar wind magnetic field by changing the Alfvén radius. The Alfvén radius,  $R_A$ , is defined as the point where the Alfvén Mach number is equal to unity — i.e.,  $M_A \equiv u_{sw}/v_A=1$ , where  $u_{sw}$  is the stellar wind speed and  $v_A$  is the Alfvén speed. Interior to  $R_A$  (the sub-Alfvénic wind) the magnetic field of the star is mostly radial, and corotates at the angular rate of the star; exterior to  $R_A$  (the super-Alfvénic wind) the field begins to lag behind corotation as the magnetic tension is overcome by the flow of the wind. In the super-Alfvénic regime, the interplanetary magnetic field (IMF) exhibits the well-known Parker-spiral (Parker 1958). The Alfvén point is an important boundary that modifies the energy transfer between the stellar wind and the planetary magnetosphere.

To estimate the Alfvén radius, we note that Proxima Centauri rotates approximately  $\sim 19$  times more slowly than EV Lacertae. To correctly estimate the interactions, we must place Proxima b at an orbital distance with proper wind conditions — including the sub-(super-) Alfvénic flow — i.e., we must consider where Proxima b orbits relative to its Alfvén radius,  $R_A$ . For our purposes, we estimate an average  $R_A$  for a simple stellar dipole moment:

$$R_A = \left( \frac{4\pi\mathcal{M}_*^2}{\dot{M}_*\omega_*\mu_0} \right)^{\frac{1}{5}}, \quad (1)$$

where  $\mathcal{M}_*$  is the magnetic dipole moment for the star,  $\dot{M}_*$  is the mass-loss rate,  $\omega_*$  is the angular frequency of stellar rotation, and  $\mu_0$  is the vacuum permeability. For EV Lacertae and Proxima Centauri,  $R_A$  are  $\sim 65.4$  and  $115 R_*$ , respectively. This is the average value for a simple dipole moment, as we are not including magnetic topology, but nonetheless the value obtained for EV Lac agrees well with the approximate average for the more complicated magnetic treatment simulated in Cohen et al. (2014). The relative orbit for Proxima b is therefore  $\sim 0.76 R_A$ . Coincidentally, this corresponds well to the simulated Planet B at EV Lac in Cohen et al. (2014), which orbits at  $\sim 0.79 R_A$ . Note that our calculated estimate of  $R_A$  does not take into account the complicated magnetic topology of a realistic stellar magnetic field, so the planet likely orbits through sub- and super-Alfvénic conditions (e.g., Fig. 1 of Cohen et al. (2014)). Therefore, we consider both super- and sub-Alfvénic conditions for the steady-state stellar wind, using the reported parameters at Planet B from Cohen et al. (2014); see Table 1.

TABLE 1  
STELLAR WIND CONDITIONS

Quantity	Sub-Alfvénic	Super-Alfvénic
$n$ ( $\text{cm}^{-3}$ )	433	12895
$T$ ( $10^5$ K)	3.42	4.77
$\mathbf{u}$ ( $\text{km s}^{-1}$ )	(-630, -1, 30)	(-202, 102, 22)
$\mathbf{B}$ (nT)	(-804, 173, 63)	(-57, 223, 92)
$M_A$	0.73	4.76

NOTE. — Stellar wind conditions from Cohen et al. (2014).

### 2.2. Auroral stellar wind power scaling

The stellar wind power delivered to the magnetosphere of the planet can be expressed as

$$P_{SW} = \rho v^3 \pi R_{MP}^2, \quad (2)$$

where  $\rho$  and  $v$  are the stellar wind mass density and velocity, respectively, and  $R_{MP}$  is the magnetopause distance along the line connecting the star and planet (sub-stellar point). The latter can be estimated through magnetospheric pressure balance with the total stellar wind pressure:

$$\frac{\mathcal{M}^2}{2\mu_0 R_{MP}^6} = p_{KE} + p_{ram} + p_B, \quad (3)$$

where  $\mathcal{M}$  represents the magnitude of the magnetic dipole moment and  $R_{MP}$  is the distance from the planet at which the magnetic pressure of the planet balances the pressure of the stellar wind. The terms on the RHS of Eq. 3 represent the kinetic ( $p_{KE} = nk_B T$ ), dynamic ram ( $p_{ram} = \rho v^2$ ), and magnetic ( $p_B = B_{SW}^2/2\mu_0$ ) pressures of the stellar wind, calculated from the values in Table 1. For the Earth-like, EL, (Neptune-like, NL) magnetosphere, we assume a magnetic dipole moment of  $\mathcal{M} = 8.0 \times 10^{15}$  ( $2.2 \times 10^{17}$ ) Tesla  $\text{m}^3$ . Solving for  $R_{MP}$  in Eq. 3 and inserting into Eq. 2 provides an estimate of the stellar wind power incident on the planetary magnetopause. Externally-driven planetary auroral systems are not typically 100% efficient at converting the incident stellar wind power into electromagnetic auroral emission, and range from  $\sim 0.3\%$  at Neptune,  $\sim 1\%$  at Earth, and up to  $\sim 100\%$  at Jupiter (e.g. Cheng 1990; Bhardwaj & Gladstone 2000). For reference, at Earth, this method gives us a reasonable estimate of the total emitted electromagnetic auroral power of  $\sim 30$  GW for nominal solar wind conditions ( $4 \text{ cm}^{-3}$ ,  $400 \text{ km s}^{-1}$ ,  $10 \text{ eV}$  protons), which is consistent with the anticipated power of 1-100 GW, depending on solar and magnetospheric activity. While the intensities of various emissions vary widely with activity and atmospheric conditions, we assume an averaged auroral emission. In order to estimate the emitted power of the OI 5577Å line, we assume it represents 2% of all emitted electromagnetic power (Chamberlain 1961; Kivelson & Russell 1995), as calculated by Eq. 2.

Fig. 1 shows the predicted emitted power of the 5577Å line based on Eq. 2 and scaled by the 2% factor mentioned above and by the conversion efficiencies for the different cases we consider (EL and NL dipoles; sub- and super-Alfvénic stellar wind conditions). For the Earth, this method predicts a value of  $\sim 0.68$  GW emission for the 5577Å line. Assuming a  $5^\circ$  latitudinal width at  $\sim 18^\circ$  co-latitude, this corresponds to a photon flux of  $\sim 13.6$  kR

TABLE 2  
CALCULATED 5577Å AURORAL POWER, BY METHOD

Case	Method 1 [TW]	Method 2 (SS) [TW]	Method 2 CME (CME+SS) [TW]
EL <sub>Sub</sub>	0.041	0.095 (0.25)	8.5 (22.4)
NL <sub>Sub</sub>	0.11	0.68 (1.8)	60.7 (160.3)
EL <sub>Sup</sub>	0.044	0.057 (0.16)	5.2 (14.2)
NL <sub>Sup</sub>	0.12	0.41 (1.1)	36.8 (101.2)

NOTE. — Power emitted for the OI 5577Å line in terrawatts (TW) for the Earth-like (EL) and Neptune-like (NL) planets in the sub-Alfvénic (Sub) and super-Alfvénic (Sup) stellar wind. For method 2, column 2, both typical and substorm (SS) values were calculated. For method 2, column 3, values for both CME + no substorm and CME + substorm (CME+SS) values are represented.

( $1 \text{ R} = 1 \text{ Rayleigh} \equiv 10^6 \text{ photons s}^{-1} \text{ cm}^{-2}$ ). This is in agreement with moderate, steady-state auroral activity (e.g. Chamberlain 1961; Steele & McEwen 1990).

Power estimates for the 5577Å line for both the EL and NL planets at 0.05 AU orbit around Proxima Centauri are shown in Table 2. For the EL planet, the emitted power is  $\sim 0.041$  (0.065) TW, and for the NL planet, the emitted power is  $\sim 0.11$  (0.12) TW in the sub-(super-) Alfvénic stellar wind. These are the estimates for a steady-state stellar wind, for a terrestrial planet with either EL or NL dipole moments. Note that discussion of a  $\sim 17.15$  Earth-mass, Neptune-like planet with an H-based atmosphere is included below in § 2.3.

This method has a weakness in that it completely ignores the incident Poynting flux from the IMF, and potential direct magnetic interactions between the stellar wind and planetary magnetic field, e.g. flux merging or reconnection. These interactions can produce a significant amount of magnetospheric energy, and so it is important to discuss a prediction that does take these into account. We do so in the next section.

### 2.3. 3D MHD empirical energy coupling

Wang et al. (2014) developed a global, 3D MHD model to obtain a nonlinear fit for the solar wind-magnetosphere energy coupling function to estimate the energy transferred from the solar wind to Earth’s magnetosphere (see their Eq. 13). As their system was focused on the Earth’s magnetosphere, we scale it to other planetary magnetic fields – such as Neptune’s – by noting the coupling scales with the planetary magnetic dipole magnitude,  $\mathcal{M}_p^{2/3}$  (Vasyliunas et al. 1982, also Eqs. 2 & 3 above). Therefore,  $(\mathcal{M}_{Nep}/\mathcal{M}_{Earth})^{2/3} \approx 9.1$ , which we can fold into the coupling constant for a NL planet.

Wang et al. (2014) estimate the fraction of total solar wind energy input to the entire magnetosphere is  $\sim 13\%$  of the incident energy. They further estimate that 12% of that energy is dissipated by particle precipitation in the auroral regions, yielding a total solar wind/auroral coupling efficiency of  $\sim 1.56\%$  – very similar to the efficiency value assumed for Earth and the EL planet in §2.2. This method provides a direct calculation of the power delivered as auroral particle precipitation given stellar wind conditions. We then translate that below into auroral emission given observed efficiencies.

As validation, we use this method to predict a maximum coupling of auroral particle precipitation (with

IMF clock angle  $\theta = \pi$ , driving reconnection and likely substorm activity) at Earth (Neptune) of  $\sim 0.21$  (0.003) TW for nominal solar wind conditions at those planets. This is of order of magnitude agreement with terrestrial plasma observations during highly energetic events (e.g. Hubert et al. 2002) and inferred values from Voyager UV measurements (e.g. Sandel et al. 1990; Mauk et al. 1994).

For Proxima b subjected to the stellar winds from Table 1, this method predicts a total power of auroral particle precipitation of  $\sim 10.7$  (97.5) TW for the EL (NL) planet in the sub-Alfvénic stellar wind, and  $\sim 6.5$  (59.2) TW in the super-Alfvénic wind. For magnetospheric substorm conditions, we predict  $\sim 28.3$  (257.7) TW for the EL (NL) planet in the sub-Alfvénic wind, and 17.9 (162.6) TW for the EL (NL) planet in the super-Alfvénic stellar wind. To compare directly to the 5577Å line auroral power output such as that calculated in §2.2, we must link these values to the aurora by including the efficiency of precipitating charged particles in the production of auroral emission for the 5577Å line, as below.

To calculate the photon flux, we use the reported values from Steele & McEwen (1990), who used ground-based observations of auroral line intensities and the related satellite observations of energetic electron flux to draw a relation between electron precipitation and auroral photon flux. We then integrate the resulting flux over a nominal  $5^\circ$  auroral oval (for each hemisphere), the colatitude of which is dependent on the sub-stellar magnetopause distance. This gives us the total output power of the 5577 Å line.

Steele & McEwen (1990) reported the conversion efficiency for the 5577Å OI line as  $1.73 \pm 0.51$  ( $1.23 \pm 0.44$ )  $\text{kR}/(\text{erg cm}^{-2} \text{s}^{-1})$  for a magnetospheric Maxwellian electron population of characteristic temperature 1.8 (3.1) keV. In the present work, we take the average values for these populations,  $\sim 1.48 \text{ kR}/(\text{erg cm}^{-2} \text{s}^{-1})$ . The magnetopause distance we calculate via Eq. 3 for the EL (NL) magnetic dipole moment is similar for both sub- and super-Alfvénic conditions, with an average value  $\sim 3.9$  (11.35)  $R_P$ , and can provide a simple estimate of the total auroral oval coverage. The magnetic colatitude of the boundary between open and closed flux is  $\sin^{-1}(1/\sqrt{R_{MP}})$ ; if we assume a nominal  $5^\circ$  auroral oval width centered at the co-latitude obtained, we calculate a single-hemisphere coverage of  $\sim 1.12 \times 10^{17}$  ( $6.62 \times 10^{16}$ )  $\text{cm}^2$  for the auroral oval of the EL (NL) planet.

Following the above, we obtain a photon flux value of 2.37 (36.53) MR for the EL (NL) planet for the 5577Å line for the sub-Alfvénic wind, and 1.44 (22.18) MR for the super-Alfvénic conditions. This corresponds to our predicted emission power in Table 2 of  $\sim 0.095$  (0.68) TW for the EL (NL) planet under steady-state sub-Alfvénic conditions, and  $\sim 0.057$  (0.41) TW under steady-state super-Alfvénic winds. For the maximum emission during a magnetospheric substorm, we obtain values of  $\sim 0.25$  (1.8) TW for sub-Alfvénic winds, and  $\sim 0.16$  (1.1) TW for super-Alfvénic winds.

There is another case of interactions that we should mention here that involves stellar activity — flaring and coronal mass ejections (CME). In these cases, stellar wind densities could increase by a factor of  $\sim 10$ , velocities by a factor of  $\sim 3$ , and IMF magnitude by a factor of  $\sim 10 - 20$  (Khodachenko et al. 2007; Gopalswamy

et al. 2009). Inserting such ratios in the the treatment by Wang et al. (2014), we predict transient maximum 5577Å emissions of  $\sim 8.5$  (60.7) TW for the EL (NL) planet under sub-Alfvénic CME conditions, and  $\sim 5.2$  (36.8) TW under super-Alfvénic CME conditions. For the maximum emission during a magnetospheric substorm under CME conditions, we obtain values of  $\sim 22.4$  (160.3) TW for sub-Alfvénic winds, and  $\sim 14.2$  (101.2) TW for super-Alfvénic winds. These transient, CME conditions can have timescales of  $\sim 10 - 10^3$  minutes per event, with multiple, consecutive events possible. Given that Davenport et al. (2016) report such high stellar activity for Proxima Centauri, Proxima b could experience CME impacts for a large percentage of its orbital phase (e.g., Khodachenko et al. 2007).

If Proxima b is, instead, a planet of Neptune mass and radius (as opposed to our assumption of only the magnetic parameters) on a close to face-on orbit, it will have an upper atmosphere dominated by H/H<sub>2</sub>. Therefore the above calculations are not applicable, and we should consider FUV emission in lieu of the OI line. Voyager UV observations reported by Sandel et al. (1990) estimated the localized FUV (967-1115 Å) auroral photon flux as  $\sim 5 R$ . Mauk et al. (1994) found that the electron flux to drive the observed UV aurora at Neptune was  $\sim 10^{-3} \text{ erg cm}^{-2} \text{ s}^{-2}$ . Therefore we infer a conversion efficiency for Neptune’s aurora in the 967-1115 Å bandpass to be  $\sim 5 \text{ kR}/(\text{erg cm}^{-2} \text{ s}^{-1})$ , corresponding to  $\sim 9.9\%$ . This gives us a scaled FUV photon flux of  $\sim 4.02$  (2.44) MR for the sub-(super-) Alfvénic stellar wind conditions for the Neptune-like planet, or 15.63 (9.49) TW over the 967-1115 Å band. While this is significantly stronger than the OI emission of an Earth-like planet, it may be harder to detect given both the width of this band and the fact that if Proxima b is Neptune-like, its orbital inclination must be  $\lesssim 5^\circ$ , making deconvolution from stellar lines more difficult (see §4). Note that Neptune’s magnetic field is highly inclined, rotationally offset, and relatively complex with significant quadrupole/octupole moments that have similar or higher magnitude than the dipole moment; in the present work, we have assumed a simple, untilted dipole field, with a magnetic moment equal to that reported by Voyager 1 observations (e.g. Connerney et al. 1991; Mauk & Bagenal 2012).

The preceding estimates are conservative. It is possible that all the auroral numbers reported for the sub-Alfvénic cases above could be a factor of 4-5 (or more) larger. We are assuming a simple dipolar, Earth-Sun like interaction with the sub-Alfvénic stellar wind, which isn’t specifically the case for sub-Alfvénic flow; these interactions are more akin to the interactions of Ganymede and Io with the corotating magnetosphere of Jupiter, with the formation of Alfvén wings. Modeling efforts by Preusse et al. (2007) showed that for a giant planet with a dipole magnetic moment, field-aligned currents (which are associated with auroral activity) are significantly stronger for planets orbiting inside the Alfvén radius of their stellar host. Our estimates, therefore, could be viewed as lower limits. It is also worth noting that Cohen et al. (2014) suggested that a transition between the sub- and super-Alfvénic conditions would likely produce enhanced magnetospheric activity and therefore could lead to a periodicity in the auroral activity depending on com-

binned planetary orbital and stellar rotational phases. For Earth, the diffuse airglow at  $5577\text{\AA}$  can be significant ( $\geq 1$  kR), but the anticipated magnitude at Proxima b is unknown, and could be another factor that contributes to the overall signal. Detailed photochemical modeling is required to obtain an estimate of airglow production.

In summary, we predict a steady-state auroral emission at  $5577\text{\AA}$  from Proxima b that is of order 100 times stronger than seen on Earth for a quiet magnetosphere, corresponding to an emitted auroral power for the OI line on the order of  $\sim 0.065$  TW, averaged over methods 1 and 2 for a quiet magnetosphere. Assuming Proxima b is an Earth-like terrestrial planet, our maximum transient power estimate for the  $5577\text{\AA}$  line for CME conditions that drive a magnetospheric substorm is  $\sim 22.4$  TW, or  $\sim 35,000$  times stronger than on Earth. The actual values for Proxima b will naturally change based on planetary parameters (e.g., magnetic dipole moment, magnetospheric particle energy distributions, substorm onset, atmospheric Joule heating) and stellar activity. By our analysis, a  $\sim 10^3$  (or higher) enhancement compared to Earth as suggested by O’Malley-James & Kaltenegger (2016) is only possible due to one or more of the following: transient magnetospheric conditions driven by either CME or substorm activity, a magnetic dipole significantly stronger than Earth’s, or higher stellar mass-loss than predicted (Wood et al. 2005; Cohen et al. 2014).

### 3. AURORAL DETECTABILITY

In this section we assess the detectability of the  $5577\text{\AA}$  OI auroral emission line from the atmosphere of Proxima b. Below, we investigate the line profile shape and then calculate planet-star contrast ratios and integration times required for auroral detection.

#### 3.1. OI Auroral Line Profile

To estimate the signal-to-noise as a function of spectral resolution, we need to estimate the auroral spectral line width. The OI  $5577\text{\AA}$  green line has no hyperfine structure and negligible natural width (Hunten et al. 1967). Spectroscopic observations of the OI airglow by Keck/HIRES (Slanger et al. 2001) and by HARPS (Anglada-Escudé et al. 2016, see §4) are unresolved, revealing the resolution element width of the instrument used for the observation at the wavelength of the line ( $\sim 0.1\text{\AA}$  Keck/HIRES;  $\sim 0.05\text{\AA}$  HARPS) rather than the true full width at half max (FWHM) of the line.

To determine the width of the line, we examine several line broadening mechanisms that play a key role in terrestrial atmospheres. The planet’s rotation will broaden the OI line, but calculations by Barnes et al. (2016) and Ribas et al. (2016) show that Proxima b is likely tidally locked with a rotation period of 11.2 days, resulting in negligible rotational broadening ( $FWHM = 0.002\text{\AA}$ ). Pressure broadening can also be safely neglected since OI auroral emission occurs in terrestrial atmospheres at an elevation of  $\sim 100$  km where the atmosphere is thin (Slanger et al. 2001). Doppler broadening should therefore be the dominant line broadening mechanism, resulting in a Gaussian line profile. For the  $5577\text{\AA}$  OI line,

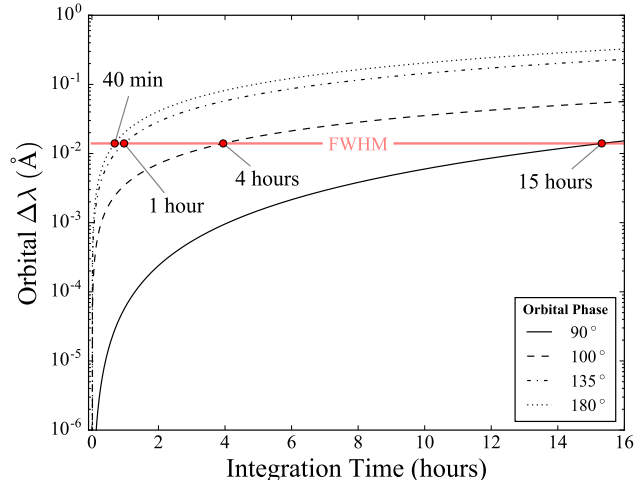


FIG. 2.— Orbital broadening of the  $5577\text{\AA}$  OI line as a function of the exposure time for observations made at different orbital phases:  $90^\circ$  (quadrature),  $100^\circ$ ,  $135^\circ$ , and  $180^\circ$  (full phase). The FWHM given by Eq. 4 is indicated by a horizontal red line; the intersection of this line with the black curves corresponds to the integration time for which the FWHM doubles. At quadrature, exposures up to  $\sim 6$  hours long have a negligible effect ( $\Delta\lambda \lesssim 10^{-3}\text{\AA}$ ) on the width of the line. At all other phases, the broadening is larger and can cause a significant increase in the FWHM in  $\sim 1$  hour.

Doppler broadening gives the following scaling relation:

$$FWHM = 2\Delta\lambda = 0.014 \left( \frac{T}{200 \text{ K}} \right)^{1/2} \text{\AA}, \quad (4)$$

where  $T$  is the temperature of the emitting layer, for which we adopt the value of 200 K (c.f. Slanger et al. 2001). A FWHM of  $0.014\text{\AA}$  is in good agreement with the Fabry-Perot interferometric line width measurements of Wark (1960).

Given the relatively short period of Proxima b, we must also consider the possibility of broadening due to the orbital motion of the planet over the course of an observation. In Fig. 2 we plot the orbital broadening of the  $5577\text{\AA}$  line as a function of the exposure time, calculated from the maximum change in the radial velocity of the planet over the course of the observation and assuming an inclination of  $90^\circ$ . The effect is strongest at full and new phases (dotted line), where the time derivative of the radial velocity is highest, and weakest at quadrature (solid line), where the derivative is smallest. Two intermediate phases are also shown. The FWHM given by Eq. 4 is indicated by a horizontal red line; orbital broadening becomes significant as the curves approach this line. In general, observations made at quadrature with exposure times up to  $\sim 6$  hours cause negligible broadening. At all other phases, however, broadening becomes significant in a matter of one or a few hours. At full and new phase, the line width doubles after an exposure of only 40 minutes. However, at these phases the radial velocity of the planet relative to the star is zero, and as we argue in §4 below, disentangling stellar and planetary emission becomes difficult. In the discussion that follows, we therefore focus on observations made close to quadrature.

Fig. 3 shows a high-resolution model spectrum of Proxima b at quadrature, illustrating an auroral emission fea-

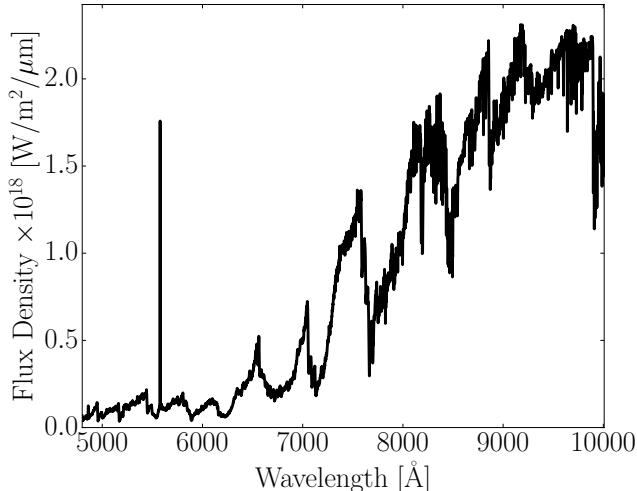


FIG. 3.— Simulated high-resolution visible spectrum of Proxima b with a 0.065 TW OI auroral emission at 5577 Å. A grey geometric albedo of 0.3 is assumed for the planet. The spectrum is calculated at quadrature phase and scaled to the observing distance (1.302 pc).

ture that could be expected from the planet. We injected a Gaussian line at 5577 Å with  $\text{FWHM} = 0.014 \text{ \AA}$ , normalized to a steady-state Proxima b OI auroral power of  $L_{OI} = 0.065 \text{ TW}$ . The OI auroral power yields an equivalent width of  $\sim 3.54(L_{OI}/1 \text{ TW}) \text{ \AA}$  relative to our model of the reflected planetary spectrum at quadrature.

### 3.2. Contrast Ratios & Telescope Integration Times

To unambiguously detect a narrow emission feature, such as the example shown in Fig. 3, the effect of telescope resolving power ( $R \equiv \lambda/\Delta\lambda$ ) needs to be taken into account. The typical resolving power being considered for future space-based coronagraph mission concepts is  $R \approx 100$ , which is appropriate for the detection of molecular absorption bands in the optical and NIR given the relatively low planet-star contrast ratio (Robinson et al. 2016). However, at 5577 Å an  $R = 100$  spectrograph has a spectral element width of  $\Delta\lambda \approx 56 \text{ \AA}$ , over  $\sim 10^3$  times broader than the OI green line width. Future space-based high-contrast exoplanet imaging missions would need to fly with higher resolution spectrographs to detect the OI 5577 Å line.

Fig. 4 shows planet-star contrast ratios in a spectral element centered on the 5577 Å OI auroral line as a function of spectrograph resolving power and auroral power, assuming a FWHM of 0.014 Å (i.e., negligible orbital broadening). The FWHM of the auroral line and equivalent width ( $W_\lambda$ ) as a function of auroral power are represented as “resolving powers,” where  $R_{FWHM} = \lambda_{OI}/FWHM$  and  $R_W = \lambda_{OI}/W_\lambda$ , respectively. Planet-star contrast gains only occur when the width of a spectral element is smaller than the equivalent width. For resolving powers greater than  $R_{FWHM}$ , multiple spectral elements are needed to span the emission line, which may introduce additional unwanted read noise and dark current. Therefore, observations should be made in the wedge between the FWHM resolving power and the equivalent width resolving power. Our predicted steady-state auroral emission ( $\sim 0.1 \text{ TW}$ ) requires that spectrographs achieve  $R \gtrsim 10^5$ .

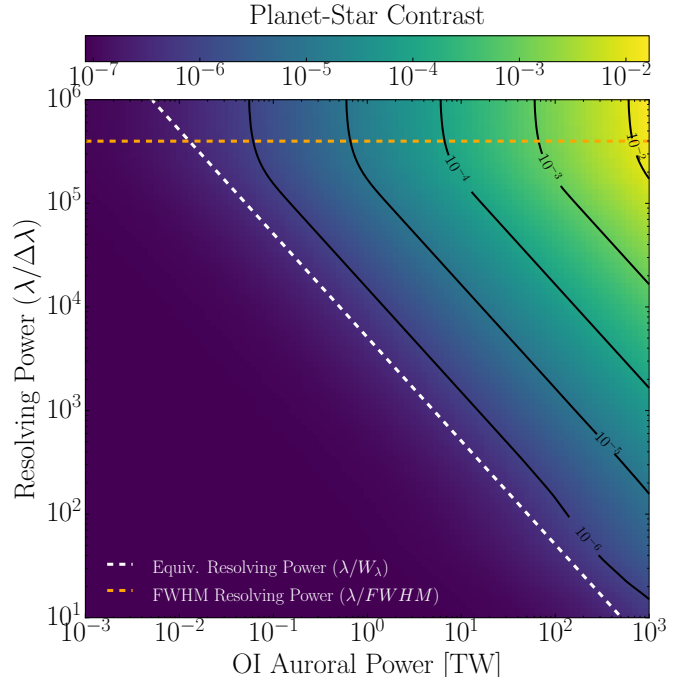


FIG. 4.— Planet-star contrast ratio contours as a function of telescope resolving power and OI auroral power. The full width at half max (FWHM; dashed-orange) of the line and equivalent width ( $W_\lambda$ ) as a function of auroral power (dashed-white) are represented as “resolving powers”, where  $R_{FWHM} = \lambda_{OI}/FWHM$  and  $R_W = \lambda_{OI}/W_\lambda$ , respectively.

Using the auroral power estimates from §2, we explore the feasibility of detecting the 5577 Å OI auroral emission line with five different ground-based telescope configurations: the 3.6m High Accuracy Radial velocity Planet Searcher (HARPS), the 8.2m Very Large Telescope (VLT) with and without a coronagraph, and a Thirty Meter Telescope (TMT) concept with and without a coronagraph (Skidmore et al. 2015; Udry et al. 2014; Johns et al. 2012). We also model the detection using two future space-based coronagraph concepts: the 16m Large UV/Optical/IR Surveyor (LUVOIR; Kouveliotou et al. 2014; Dalcanton et al. 2015) and the 6.5m Habitable Exoplanet Imaging Mission (HabEx; Mennesson et al. 2016).

High spectral resolution coronagraphy with the VLT will require an update to the SPHERE high-contrast imager and a coupling with the ESPRESSO spectrograph, as described in Lovis et al. (2016). Note that given the VLT’s 8.2m diameter, the SPHERE coronagraph must achieve an inner working angle no more than  $\theta_{IWA} = 2.7\lambda/D$  to extend as long as 5577 Å given the maximal planet-star angular separation of 37 mas for Proxima b. Our HARPS, TMT, LUVOIR and HabEx telescope models use  $R = 115,000$ , while for VLT we use  $R = 120,000$ . All models assume a total throughput of 5% and a quantum efficiency of 90%. Coronagraph noise estimates use the model presented in Robinson et al. (2016) with updated parameters from Meadows et al. (2016), and consider noise due to speckles, dark counts, read noise, telescope thermal emission, and zodi and exozodi light. Ground-based coronagraphy assumes a conservative design contrast of  $10^{-5}$  (Dou et al. 2010; Guyon et al. 2012), while space-based assumes  $10^{-10}$  (Meadows

TABLE 3  
 PLANET-STAR CONTRAST RATIOS AND TELESCOPE INTEGRATION TIMES NECESSARY TO DETECT THE 5577Å OI AURORAL LINE

Power [TW]	Contrast	Telescope Integration Time [hours]							
		HARPS	VLT	VLT + C	TMT	TMT + C	HabEx	LUVOIR	TMT + C*
0.001	$9 \times 10^{-8}$	$2 \times 10^{13}$	$4 \times 10^{12}$	$4 \times 10^8$	$3 \times 10^{11}$	$1 \times 10^7$	$6 \times 10^8$	$2 \times 10^7$	$1 \times 10^5$
0.01	$2 \times 10^{-7}$	$2 \times 10^{11}$	$4 \times 10^{10}$	$4 \times 10^6$	$3 \times 10^9$	$1 \times 10^5$	$6 \times 10^6$	$2 \times 10^5$	$2 \times 10^3$
0.1	$8 \times 10^{-7}$	$2 \times 10^9$	$4 \times 10^8$	$4 \times 10^4$	$3 \times 10^7$	$1 \times 10^3$	$6 \times 10^4$	$2 \times 10^3$	40
1	$7 \times 10^{-6}$	$2 \times 10^7$	$4 \times 10^6$	$4 \times 10^2$	$3 \times 10^5$	10	$7 \times 10^2$	30	3
10	$7 \times 10^{-5}$	$2 \times 10^5$	$4 \times 10^4$	7	$3 \times 10^3$	$4 \times 10^{-1}$	10	1	$3 \times 10^{-1}$
100	$7 \times 10^{-4}$	$2 \times 10^3$	$4 \times 10^2$	$4 \times 10^{-1}$	30	$3 \times 10^{-2}$	$6 \times 10^{-1}$	$9 \times 10^{-2}$	$3 \times 10^{-2}$
1000	$7 \times 10^{-3}$	20	4	$3 \times 10^{-2}$	$3 \times 10^{-1}$	$3 \times 10^{-3}$	$6 \times 10^{-2}$	$9 \times 10^{-3}$	$3 \times 10^{-3}$

NOTE. — Integration times refer to the time required to achieve a signal-to-noise of 6 on the auroral emission above the continuum assuming a telescope throughput of 5%, a spectrograph with resolution  $\lambda/\Delta\lambda = 115,000$  for HARPS, TMT, HabEx and LUVOIR and  $\lambda/\Delta\lambda = 120,000$  for VLT. “+ C” indicates the use of a coronagraph and associated noise sources discussed in Robinson et al. (2016). Auroral power of order 0.1 TW corresponds to the predicted steady-state value in §2 while  $\sim 1 - 100$  TW corresponds to our predicted auroral power arising from a combination of substorm event and CMEs. TMT + C\* denotes a coronagraph-equipped TMT concept with a design contrast of  $C = 10^{-7}$  and negligible instrumental noise.

et al. 2016) unless stated otherwise. Integration times longer than one hour require multiple readouts, which introduces more detector noise. Non-coronagraph telescope calculations assume only stellar noise at the photon limit; their values are therefore lower limits, and may increase significantly due to stellar activity (see §4). To prevent significant orbital broadening, we assume that observations are made for one hour at a time at or close to quadrature; longer exposure times are achieved by stacking multiple observations. For exposure times much longer than an hour, stacking will appreciably increase the read noise and dark current for coronagraph observations, where the star is nulled, but not for the non-coronagraph observations, where the stellar photons dominate the noise budget.

Our integration time calculations follow those described in Robinson et al. (2016). For the stellar spectrum we adopt the steady-state Proxima Centauri spectrum of Meadows et al. (2016) and neglect the impact of flares on the stellar continuum. We assume that the quoted auroral power emitted via the 5577Å OI line is constant throughout the entire observation.

For observations without a coronagraph, both the stellar flux and reflected stellar flux define the continuum from which we wish to resolve the auroral emission feature. Observations with a coronagraph need only resolve the auroral emission above the coronagraph noise and reflected stellar continuum. With these considerations in mind, we simulate the net planetary emission as a combination of reflected stellar continuum and auroral emission. We compute the flux from the reflected stellar continuum by assuming that the planet is a Lambertian scatterer at quadrature with a planetary geometric albedo of 0.3 and a planetary radius of  $1.07R_{\oplus}$  following Barnes et al. (2016). We then inject the expected flux from the auroral line at its central wavelength. We integrate over all spectral elements that contain the auroral line flux, taking the auroral photon count rate as our signal and all other sources as noise as in Robinson et al. (2016). For the oxygen 5577Å line width of  $\sim 0.014\text{Å}$  (§ 3.1) and our nominal resolving power, this corresponds to one spectral element.

Table 3 shows the integration times required to achieve a signal-to-noise of 6 on the 5577Å OI auroral emission line above the stellar and reflected planetary continuum

as a function of auroral power. We simulated contrast ratios and integration times for emitted auroral powers at the OI 5577Å line ranging from  $10^{-3} - 10^3$  TW to bracket all potential auroral fluxes. The  $10^{-3}$  TW lower limit corresponds to a strong 5577Å emission from Earth (Earth total electromagnetic auroral power is of order  $10^{-2}$  TW with 5577Å typically  $\sim 2\%$  of this value). The upper limit of  $10^3$  TW is an extreme case that is an order of magnitude stronger than the largest value predicted in §2. Values in between correspond to the different cases considered in Table 2, which depend on the planetary dipole moment, magnetospheric substorm activity, and whether CME conditions are present. For reference, the estimated steady-state Proxima b value calculated in §2 is  $\sim 0.1$  TW.

The weak  $10^{-3}$  TW aurora is indistinguishable from the purely reflecting planet-star contrast near the 5577Å OI auroral emission line (Turbet et al. 2016; Meadows et al. 2016) and effectively demonstrates why high resolution spectroscopy is not typically considered for high-contrast imaging. For an Earth-like planet, the auroral power estimates from §2 ( $\sim 0.1$  TW) make detecting the OI emission line infeasible with current instruments, even though the contrast ratio at the line is relatively strong ( $\sim 8 \times 10^{-7}$ ). Although unlikely, if the auroral power were much higher ( $\sim 10^3$  TW) and sustained over the period of the observation, detection of OI emission could be possible with current instruments in tens of hours. Realistically, however, these estimates suggest that current instruments are likely not capable of detecting an OI aurora on Proxima b.

For a SPHERE-ESPRESSO coupling (Lovis et al. 2016), the integration times required to detect an OI auroral line are slightly more favorable over a wide range of possible auroral powers, but still prohibitively long under most plausible circumstances. If Proxima b has a Neptune-like magnetic dipole moment, and observations were made during substorm conditions (when the power in the OI 5577Å line reaches  $\sim 1$  TW with a contrast ratio of  $7 \times 10^{-6}$ ), a coronagraph-equipped VLT would have to integrate for  $\sim 400$  hours. However, if observations coincided with periods of more vigorous stellar activity such as during a concurrent CME and substorm, the auroral output could reach  $\sim 100$  TW and contrast

ratios of  $7 \times 10^{-4}$ . An upgraded SPHERE may be able to detect this signal in under an hour. Since CMEs and fast stellar wind streams can have timescales  $\sim 10$  hours, and substorms up to several days (Gonzalez et al. 1994, 1999), the high level of transient activity may be observable. Under near constant CME activity, storm conditions could potentially last for weeks or longer, improving the chances of detecting auroral emission (Khodachenko et al. 2007).

Even future observations with TMT, HabEx, and LUVOIR outfitted with instruments optimized for high-resolution, high-contrast coronagraphy will be unable to detect a steady-state 0.1 TW OI aurora on Proxima b. However, a coronagraph-equipped TMT could detect a substorm strength aurora of  $\sim 10$  TW in about 10 hours, while LUVOIR could make the predicted substorm auroral observation in about 30 hours. Only auroral powers  $\gtrsim 10$  TW would be detectable with HabEx. Auroral powers of order 100 TW arising from a concurrent CME and substorm could be observed by the TMT, HabEx, and LUVOIR in well under an hour.

Finally, we consider how improvements in ground-based instrumentation might expand the ability to detect exo-aurorae. In the top panel of Fig. 5, we model a coronagraph-equipped TMT concept that achieves a design contrast of  $C = 10^{-7}$  and has negligible instrumental noise (e.g., no dark current and read noise). Low-resolution observations with a resolving power smaller than the equivalent width resolving power,  $R < \lambda/W_\lambda$ , yield longer integration times at fixed auroral power as the auroral signal is diluted by additional stellar continuum photons from larger spectral elements, which increases the noise. For high resolutions that exceed the equivalent width resolving power,  $R > \lambda/W_\lambda$ , the auroral signal dominates the planetary continuum as the spectral element more tightly bounds the narrow emission feature, yielding little additional improvement in integration times.

In the bottom panel of Fig. 5, we vary coronagraph design contrasts for observations with and without instrumental noise. We find that a TMT with coronagraphic starlight suppression, negligible instrumental noise, a design contrast of  $C = 10^{-7}$  and  $R > 10^5$  allows for a detection of our predicted steady-state OI auroral emission (auroral power of  $\sim 0.1$  TW) over about 40 hours (see also Table 3). The discontinuities that occur at high resolving powers are due to the need for additional spectral elements to span the width of the OI auroral line.

Despite the likely increased strength of aurorae on Proxima b compared to Earth, observing a *steady-state* 0.1 TW aurora requires sufficiently long integration times that it is not currently feasible, nor will it be feasible with the next generation of instruments, unless ideal instrumental performance were achieved. OI auroral detection may only be possible if observations coincide with magnetospheric substorms or periods of vigorous stellar activity, such as CMEs, which can induce much stronger aurorae ranging from 1 – 10 TW (and up to  $\sim 100$  TW if Proxima b has a stronger magnetic dipole than Earth). These transient events are frequent on Proxima Centauri (Davenport et al. 2016) and may persist on timescales comparable to the integration times needed to detect strong aurorae, giving a search for auroral emission a

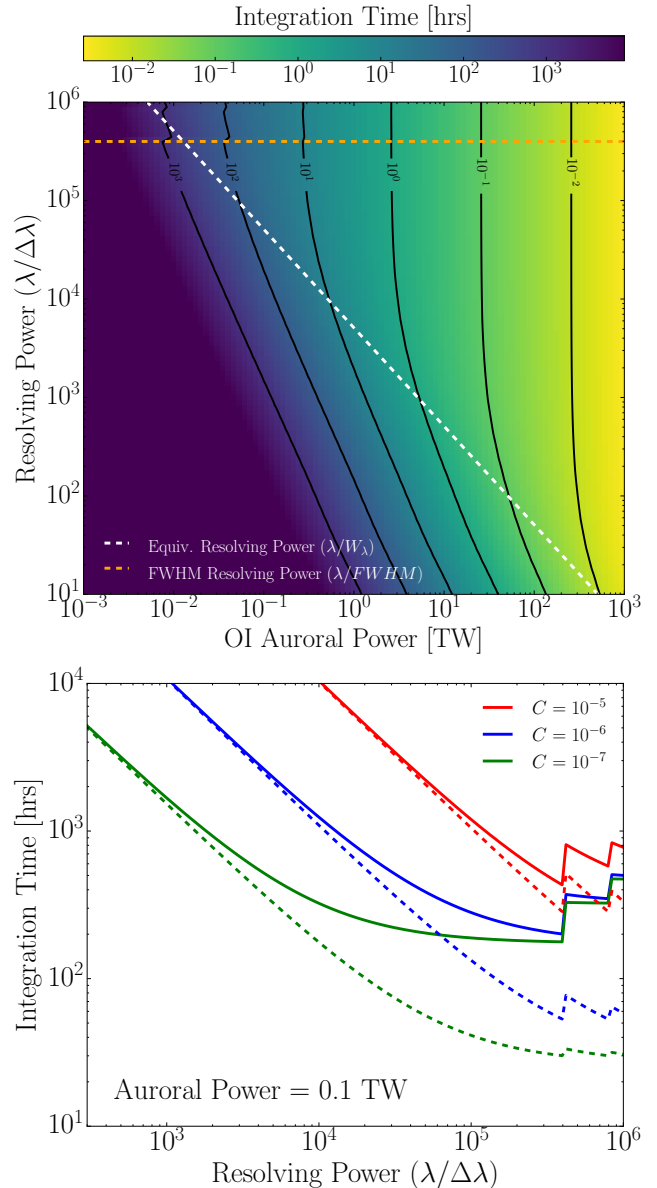


FIG. 5.— *Top*: Similar to Fig. 4, but displays telescope integration time contours as a function of telescope resolving power and OI auroral power for a coronagraph-equipped TMT concept with a design contrast of  $C = 10^{-7}$ . Dark current, read noise, and telescope thermal noise are set to zero here to simulate optimal detector performance that may be achieved by future instruments. *Bottom*: Telescope integration time as a function of resolving power for a coronagraph-equipped TMT concept for three different design contrasts. The solid curves denote integration times that include all modeled noise sources while the dashed curves assume negligible instrumental noise.

plausible chance of success.

#### 4. SEARCH IN THE HARPS DATA

The ESO Archive<sup>7</sup> hosts 319 HARPS spectra of Proxima Centauri taken between 2004 and 2016 and totaling about 70 hours of exposure time. The spectra were taken in the wavelength range 3782 – 6913Å with a resolving power  $R = 115,000$ , yielding a wavelength resolution  $\Delta\lambda \approx 0.05\text{\AA}$  at 5577Å. Each wavelength bin was oversampled by a factor of about 5. Given the estimates in

<sup>7</sup> <http://archive.eso.org/>

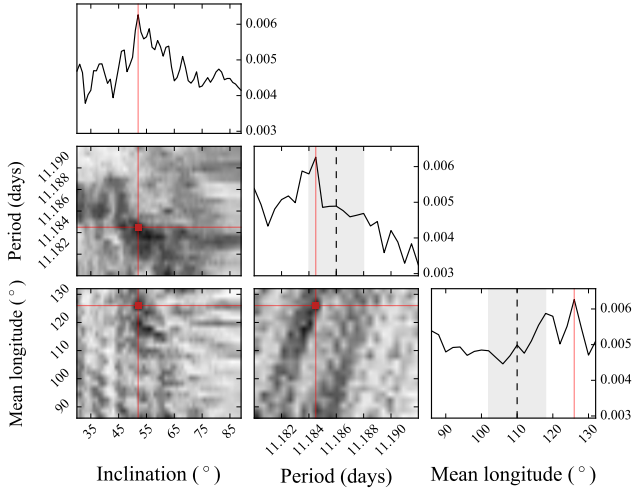


FIG. 6.— Results from the grid search over inclination ( $i$ ), period ( $P$ ), and mean longitude ( $\lambda$ ) for the strongest 5577Å planetary signal. The inclination grid spans the range  $30^\circ$ – $90^\circ$  in increments of  $1^\circ$ . The period and mean longitude grids are centered on the best-fit values reported in Anglada-Escudé et al. (2016) and span the  $\pm 3\sigma$  range in increments of  $0.25\sigma$ . In total, 37,440 different orbital configurations for Proxima b were considered. The curves along the main diagonal show the fractional amplitude of the bin centered on the OI line as a function of inclination (top left), period (center), and mean longitude (bottom right). In the period and mean longitude plots, the dashed line is the value reported in the discovery paper, with the  $1\sigma$  bounds shaded in gray. The colormaps show the joint distributions of signal strengths for pairs of the three orbital parameters (black highest, white lowest). The peak signal is indicated by the red lines and occurs at  $i = 52^\circ$ ,  $P = 11.1845$  days, and  $\lambda = 126^\circ$ , with detection significance  $\sim 0.7\sigma$ . As we argue below, this signal has a very high false alarm probability (FAP  $\sim 0.2$ ) and is entirely consistent with noise.

Table 3, if Proxima b’s auroral power were on the order of  $10^3$  TW (however unlikely), the OI line could be detectable in this dataset. We therefore downloaded all spectra to conduct a search for the OI emission feature of Proxima b. The method we outline below is similar to so-called “spectral deconvolution” techniques used to detect molecular absorption in exoplanet atmospheres (e.g., Sparks & Ford 2002; Riaud & Schneider 2007; Kawahara et al. 2014; Snellen et al. 2015).

We first shifted all spectra to the stellar rest frame by cross-correlating them against each other and calibrating the wavelength array to the stellar Na D I and II lines. Next, we removed stellar lines by performing weighted principal component analysis (WPCA; Delchambre 2015) on a  $250\text{\AA}$  window centered at  $5577\text{\AA}$ . Each spectrum was then fit with a linear combination of the first 10 principal components, a number which we obtained by optimizing the recovery efficiency of injected planetary signals (see below); the fit was then subtracted, reducing the noise in the vicinity of  $5577\text{\AA}$  by a factor of  $\sim 7$ . In order to obtain the principal components, we weighted each spectrum by the square root of its exposure time and assigned weights of zero to the individual telluric  $5577\text{\AA}$  airglow features, as these are among the strongest features in any individual spectrum and may incorrectly bias the principal components in the stellar frame. We remove Earth airglow separately below.

Next, we Doppler-shifted all spectra into the frame of Proxima b. Since the orbital inclination  $i$  is unconstrained, we performed a grid search, varying  $i$  in one

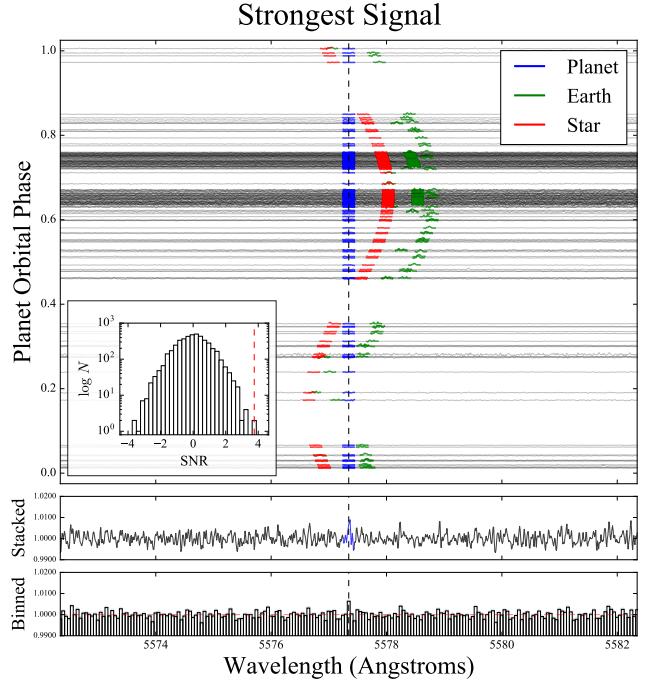


FIG. 7.— The HARPS spectra of Proxima Centauri. After removing stellar and telluric lines, the individual spectra are Doppler-shifted into the frame of Proxima b according to the orbital parameters corresponding to the peak signal in Fig. 6. The spectra are then normalized and distributed vertically on the main subplot according to the planet’s orbital phase. Blue regions indicate a small ( $0.2\text{\AA}$ ) window centered on the  $5577\text{\AA}$  oxygen feature in the planet frame. Red and green regions indicate the same window in the star and Earth frames, respectively; note the residual telluric airglow features in many of the spectra. The bottom subplots show the stacked spectrum in the planet frame and the stacked spectrum after downsampling to bins of size equal to the instrumental FWHM of the line ( $0.05\text{\AA}$ ). The peak recovered by the grid search is evident in both the stacked and the binned flux. The inset at the center left shows a histogram of the amplitude of deviations from the median in bins across a  $250\text{\AA}$  window centered on the OI line, indicating a signal-to-noise ratio (SNR) of about 4 in the  $5577\text{\AA}$  bin. Despite the apparent strength of this detection, further analysis yields a detection significance of only  $\sim 0.7\sigma$ , with false alarm probability  $\sim 20\%$  (see Fig. 9).

degree increments from  $30^\circ$  to  $90^\circ$ . We did not consider inclinations lower than  $30^\circ$  due to the difficulty of deconvolving stellar and planetary signals in near face-on orbits. We further varied the planet period  $P$  and planet mean longitude  $\lambda$  across a range spanning  $\pm 3\sigma$  about the best fit values reported in Table 1 of Anglada-Escudé et al. (2016), in increments of  $0.25\sigma$ ; in total, we considered 37,440 different orbital configurations for the planet. For simplicity, the eccentricity was assumed to be zero, the planet mass was set to  $1.27M_\oplus / \sin i$ , and the stellar mass was held fixed at  $0.12M_\odot$ . The latter parameter is considerably uncertain; however, changing the stellar mass changes the amplitude of the planetary RV signal, making the stellar mass degenerate with the inclination of Proxima b’s orbit. A grid search over the stellar mass is therefore redundant as long as we treat the inclination above as an “effective” inclination for  $M_\star = 0.12M_\odot$ .

After Doppler-shifting each spectrum, we translated them back to the original wavelength grid by linear interpolation. Once in the planet frame, we identified and interpolated over  $> 10\sigma$  outliers in each wavelength bin of the normalized spectra outside the  $0.2\text{\AA}$  window cen-

tered on the OI line. We found that this successfully removed telluric airglow and prevented outlier features in individual spectra from contributing to the stacked spectrum. We purposefully did not perform this outlier removal step in the vicinity of the (putative) planetary 5577Å line to prevent time-variable emission from being removed. Note that, in principle, this could result in a false detection of a planetary signal due to the presence of a large (non-planetary) outlier in a single spectrum. In the event that a signal were recovered, a detailed analysis of the spectrum/spectra it originated from would be necessary to rule out this possibility.

For each orbital configuration, we then co-added all spectra in the planet frame, omitting spectra in which the planetary 5577Å window overlapped with either the stellar or telluric 5577Å windows to avoid contamination from OI emission by those sources. For orbits close to edge-on, this reduced the total exposure time from 70 to about 50 hours, and less for lower inclination orbits. In order to remove correlated stellar noise, we then applied a high pass median filter of window size 1Å.

Finally, we binned the stacked spectra to 0.05Å-wide bins, with the central bin centered at 5577.345Å, the empirical wavelength of the OI green line (Cabannes & Dufay 1955; Chamberlain 1961). Our bin size is the HARPS resolution at that wavelength, and closely matches the FWHM of the telluric OI lines in the dataset. As we argued in §3, a higher resolution spectrograph (with less instrumental broadening) would allow for smaller bin sizes and higher contrast in the OI line. We then measured the amplitude of the 5577.345Å bin relative to the spectrum mean.

The results of our grid search are shown in the triangle plot in Fig. 6. Along the main diagonal, we plot the maximum fractional strength of the 5577Å signal as a function of each of the orbital parameters ( $i$ ,  $P$ , and  $\lambda$ ). Below those plots, we show the two-parameter joint distributions of the maximum signal strength, where darker colors correspond to higher values. A peak is visible at an (effective) inclination of  $52^\circ$ , a period of 11.1845 days, and a mean longitude of  $126^\circ$ . In Fig. 7 we show the spectra Doppler-shifted into the planet frame according to these orbital parameters. Each of the processed spectra are normalized and distributed vertically along the main subplot according to the planetary phase at the time the observation was made. The location of the expected OI planetary feature is indicated in blue; we show the same window in the frame of Proxima Centauri (red) and Earth (green), where residual telluric emission is clearly visible. As mentioned above, spectra in which Proxima b’s 5577Å window overlaps with either the stellar or telluric windows are omitted. When stacking the spectra below, we also we masked and interpolated over 0.2Å windows centered on the telluric features.

The stacked flux in the planetary frame is shown below the main plot, where the peak at 5577Å is visible. Below it, we show the stacked flux binned to 0.05Å bins; the feature also stands out here. The inset at the bottom left of the main subplot shows a histogram of the SNR of all the bins in a 250Å window centered on the OI line; the 5577Å feature (indicated by a dashed red line) is one of only two with SNR  $\sim 4$ . However, this signal

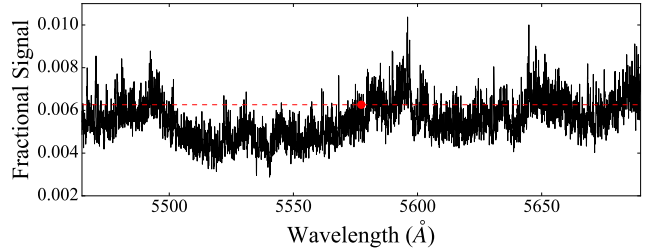


FIG. 8.— The peak signal in each wavelength bin in the vicinity of the 5577Å line. The fractional signal ( $y$  axis) is the flux in the bin divided by the continuum, and would roughly correspond to a planet-star contrast ratio if the signal were real. The peak signal at the 5577Å line ( $0.7\sigma$ ) is indicated by the dashed red line. About 20% of the bins display stronger peak signals than the 5577Å bin, leading to a FAP for the 5577Å signal of  $\sim 20\%$ . Note also the strong correlated noise as a function of wavelength, likely due to improperly subtracted time-variable stellar features.

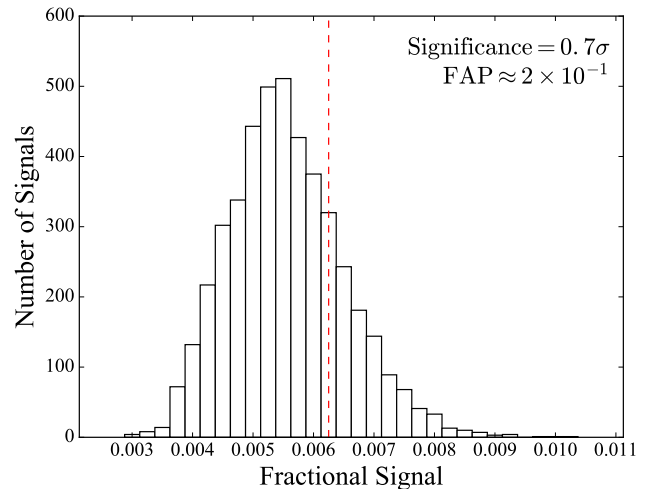


FIG. 9.— The distribution of the signal strength over the wavelength grid in Fig. 8. The bin corresponding to the peak 5577Å signal is indicated with a red dashed line; given the large FAP, the recovered signal is fully consistent with noise.

is consistent with correlated stellar noise and is in no way a detection of planetary 5577Å emission. To show this, we performed the same grid search used to generate Fig. 6 in each of 2,250 wavelength bins on either side of 5577Å (where we do not expect significant planetary emission) and computed the strongest recovered signal in each wavelength bin. The results are shown in Fig. 8, where the 5577Å bin is indicated by a red circle. The dashed red line indicates the fractional strength of the signal in that bin,  $\sim 0.006$ , which roughly corresponds to a planet-star contrast of the same magnitude if the signal were real. However, it is clear from the figure that over 20% of the bins in the range 5465 – 5670Å have a stronger peak signal than that in the 5577Å bin, from which we estimate a detection significance of  $\sim 0.7\sigma$  and a false alarm probability (FAP) for our recovered peak of  $\sim 0.2$ . These data are also shown as a histogram in Fig. 9, where the number of signals are plotted as a function of their fractional strength. It is evident from these figures that the peak shown in Fig. 7 is fully consistent with noise.

A striking feature of Fig. 8 is the correlated nature of

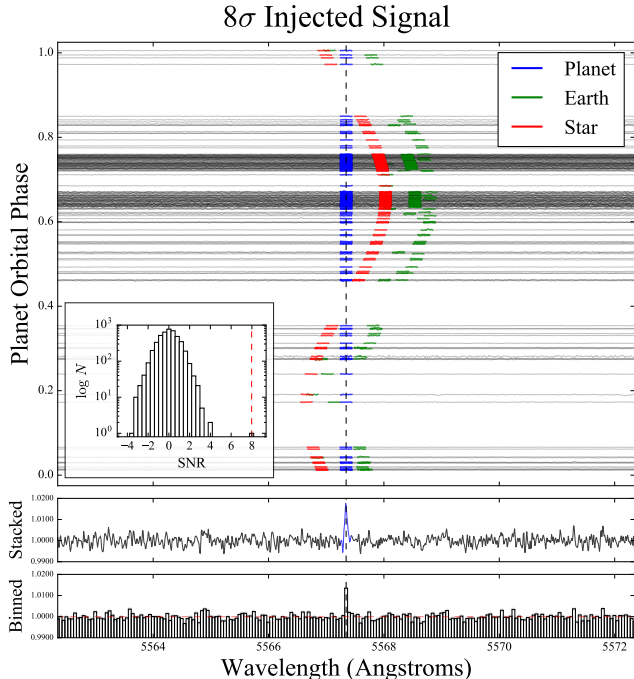


FIG. 10.— Similar to Fig. 7, but for an emission feature injected into the raw data at  $5567.345\text{\AA}$  ( $10\text{\AA}$  blueward of the OI line, where no emission is expected) with contrast  $1.8 \times 10^{-2}$ . Our method recovers the signal in the stacked, binned spectrum with  $\text{SNR} \sim 8$  and a detection significance of  $8\sigma$ , our nominal detection threshold. The non-detection in Fig. 7 therefore constrains the auroral power on Proxima b to be  $\lesssim 3 \times 10^3$  TW, consistent with the calculations in §2.

the noise; for instance, no bins in the range  $5500 - 5575\text{\AA}$  have particularly strong signals, while the  $5577\text{\AA}$  peak is one of many in its immediate vicinity. This is likely a sign of correlated stellar noise that was improperly removed by PCA, either due to high temporal stellar variability or nonlinear correlations across the spectrum that cannot be captured by PCA. At present, this noise is the limiting factor in our ability to recover auroral emission by Proxima b. Future coronagraphic observations of Proxima Centauri (§3) should greatly reduce this noise by nulling most of the starlight.

In order to quantify the constraints our non-detection imposes on the properties of Proxima b, we inject Gaussian OI emission signals with FWHM  $0.05\text{\AA}$  and of varying contrast into each of the raw spectra and attempt to recover them via the procedure described above. We find that an OI auroral signal with planet-star contrast  $1.8 \times 10^{-2}$  yields a detection with  $\text{SNR} \sim 8$  (Fig. 10). By performing the same wavelength search as before (Figs. 8 and 9), we estimate the significance of this detection to be  $8\sigma$ , which we conservatively choose to be our nominal detection threshold for the HARPS dataset. From Table 3, this contrast is equivalent to an OI auroral power of  $\sim 3 \times 10^3$  TW, our empirical upper limit on the strength of Proxima b’s  $5577\text{\AA}$  emission. Note that by scaling the estimates in that table, it should take only a few hours (versus the 50 hours used in the injection/recovery step) to detect such a signal with HARPS. This order-of-magnitude difference is likely related to the correlated stellar noise discussed above. Integration times for telescopes without coronagraphs may therefore be signifi-

cantly longer than the estimates quoted in that table.

Finally, we also performed similar searches for the red oxygen lines ( $6300.308$  and  $6363.790\text{\AA}$ ) and the  $3914.4\text{\AA}$  UV nitrogen line, which are prominent in Earth’s aurora, but find no significant peaks. Given the lower power in the red lines relative to the green line, and the low transmissivity of Earth’s atmosphere and lower detector efficiencies in the UV, this non-detection is consistent with the non-detection of the  $5577\text{\AA}$  feature.

## 5. DISCUSSION & CONCLUSIONS

Given the RV estimate of Proxima b’s mass of  $m \sin i \approx 1.27M_{\oplus}$ , the planet is likely terrestrial (Anglada-Escudé et al. 2016). However, due to the mass-inclination degeneracy, it is possible that Proxima b is more massive and on a close to face-on orbit. In this case, the planet could be a mini-Neptune with an atmosphere dominated by H and He rather than by oxygen-bearing species. As we discussed in §2, a search for Lyman-Werner  $\text{H}_2$  emission in the UV would be more appropriate in this case. Although broader than the lines we consider here, this emission is likely stronger (see §2), and is unlikely to be confused with stellar emission, given that it is molecular in origin. But perhaps more importantly, a robust *non*-detection of this and other H/He features could rule out a large gaseous envelope and confirm the terrestrial nature of the planet. That said, we are currently unable to efficiently probe near-face-on orbits due to the much smaller Doppler shift of the planetary lines. Observations made exclusively at quadrature, when the planet RV is highest, may help with this in the future.

In the more likely case that Proxima b is terrestrial, our HARPS search constrains its auroral power to be  $< 3 \times 10^3$  TW. This is consistent with the calculations in §2, which suggest the OI auroral power on Proxima b is likely  $\sim 0.065$  TW, or  $\sim 100\times$  that of the Earth during steady-state solar wind conditions. Those calculations, however, ignore transient increases in stellar magnetic activity, which can enhance the auroral signal and the diffuse airglow emission of the planet. As discussed in §2, transient magnetospheric activity could result in auroral power for the  $5577\text{\AA}$  line up to  $10 - 100$  TW, lasting from  $10 - 10^3$  minutes (§2.3). In addition, for a planet that is under near constant CME activity, it is possible that the storm conditions last for weeks or longer (Gonzalez et al. 1994, 1999). Spectra taken during periods of vigorous stellar activity could thus enhance the chances of detecting auroral emission.

Even if Proxima b is terrestrial, an auroral signal is not guaranteed to be present. The existence of an atmosphere is still an open question, owing to vigorous past hydrodynamic escape (Luger & Barnes 2015; Barnes et al. 2016), observed persistent stellar activity (Davenport et al. 2016) and an observationally unconstrained planetary magnetic field. Even if an oxygen-rich atmosphere is present, nitrogen may need to be present to enhance the auroral signal. On Earth, the OI green line emission results primarily from  $\text{O}_2^+$  dissociative recombination, as well as collisions with excited  $\text{N}_2$ , and direct electron impact (Strickland et al. 2000). It is unclear whether or not other molecular species could play a similar role if  $\text{N}_2$  is not the bulk atmospheric constituent. However, the detection of the  $3914\text{\AA}$   $\text{N}_2^+$  band could be

a good diagnostic in the UV, where the star is even fainter. If we assume that the power of the 3914Å nitrogen band is comparable to that of the OI line (which is typical for higher energy magnetospheric particle populations), then the planet-star contrast in the  $N_2^+$  band would be an order of magnitude greater than at 5577Å. Since the strength of the  $N_2^+$  band scales with magnetospheric parameters, stellar activity could cause strong transient features in the UV, which may be observable. Note, however, that limitations in UV detector efficiencies may complicate the detection of nitrogen and other UV aurorae.

Our integration times for the predicted steady-state 5577Å OI auroral line render its detection infeasible for current facilities. However, if key design goals are met for future coronagraphs, steady-state aurorae may be more easily detected. As shown in Fig. 4, achieving the optimal star-planet contrast ratio at the emission line requires that the width of a spectral element (resolving power) is smaller (greater) than the line’s equivalent width. For our predicted steady-state auroral emission ( $\sim 0.1$  TW), this requires future spectrographs to achieve  $R \gtrsim 10^5$ . High-resolution spectroscopy is also needed to resolve the Doppler shift of the planetary auroral emission ( $\sim 1$ Å) and place strong constraints on the eccentricity and mass/inclination of the planet. Such constraints would lead to greater confidence in the terrestrial nature of Proxima b. Furthermore, since read noise and dark current dominate the coronagraph instrumental noise budget, the development of low-noise detectors, e.g. MKIDS (Mazin et al. 2012, 2015), would significantly help the detection sensitivity and would allow such high-resolution spectroscopy to be downbinned to the lower resolution typically considered for direct exoplanet spectroscopy. For instance, if future detectors render read noise and dark current negligible, a LUVOIR concept telescope could observe a 0.1 TW OI 5577Å auroral emission feature in 100 hours as opposed to the  $2 \times 10^3$  hours for the noised observations considered in §3. In addition, low-noise detectors would make stacking short observations (required to mitigate broadening of the line due to the planet’s orbital motion) more feasible. If TMT is built with a coronagraph that can achieve a design contrast of  $10^{-7}$  and negligible instrumental noise, it could observe steady-state auroral emission ( $\sim 0.1$  TW) in a few nights. However, such an observation would require the development of an effective AO system in the optical.

Alternatively, observations made during periods of vigorous stellar activity may enhance the detectability of exo-aurorae on Proxima b. Transient magnetospheric activity could increase auroral power to 1 – 100 TW, depending on the planetary magnetic dipole strength, allowing future coronagraph-equipped TMT and LUVOIR telescopes to detect auroral emission in 1 hour or less. This is comparable to estimated CME timescales (Khodachenko et al. 2007) and much shorter than the timescales of long-lasting solar storm conditions (Gonzalez et al. 1994, 1999). Future observing missions similar to the MOST campaign (e.g. Davenport et al. 2016) could be used to characterize and monitor Proxima Centauri’s activity levels to constrain the star’s activity cycles. Such missions could aid in scheduling spectroscopic observations of Proxima Centauri. Observing the star

following a CME-like event or long duration fast solar streams could enhance detectability of the planetary auroral signal.

The methods of exo-auroral detection discussed here are not limited to Proxima b, but may be applicable to any exoplanet orbiting a nearby late-type star or brown dwarf. For example, the recently discovered TRAPPIST-1 system (Gillon et al. 2016) consists of three planets orbiting an active late M8 ultracool dwarf only 12 pc away; one planet in the system, TRAPPIST-1d, potentially lies in the habitable zone. Since TRAPPIST-1 is a later type star than Proxima Centauri, it is likely more active (e.g., West et al. 2008) and hence could generate larger particle fluxes and a stronger interplanetary magnetic field than Proxima Centauri, leading to more powerful aurorae on its planets. Additionally, TRAPPIST-1 is roughly  $5\times$  dimmer than Proxima Centauri at the OI 5577Å line, resulting in far more favorable contrast ratios. However, due to its distance, auroral emission from this system will be  $\sim 100\times$  dimmer than that from Proxima Centauri, likely making its detection infeasible. For coronagraphic observations, the distance to the TRAPPIST system would require an inner working angle smaller than the diffraction limit to extend as long as 5577Å for all known TRAPPIST-1 planets observed with a 10m class telescope, further complicating the observation.

Another planet to consider is GJ1132b, which orbits a M3.5 star 12 pc away (Berta-Thompson et al. 2015). Since it receives  $\sim 19\times$  the Earth’s flux and may have an  $O_2$  rich atmosphere (Schaefer et al. 2016), it could display strong auroral emission. However, as with the TRAPPIST-1 system, its distance makes auroral characterization difficult. Moreover, the earlier type host emits a larger fraction of its light in the optical, resulting in a poorer auroral contrast ratio.

Finally, exoplanets orbiting nearby brown dwarfs may be prime targets for exo-auroral searches. Early-type brown dwarfs display significant magnetic activity (West et al. 2008) and are significantly fainter than M dwarfs in the optical, potentially enhancing the detectability of the 5577Å signal from planets in orbit around them. Although no short-period exoplanets are currently known to orbit nearby brown dwarfs (He et al. 2016), the methods described in this paper may be used as means of exoplanet detection, as suggested by Sparks & Ford (2002). Since the stack-and-search method described in §4 does not require previous RV observations of a system, a long baseline of spectroscopic observations of nearby M dwarfs and brown dwarfs could be used to search for Doppler-shifted 5577Å OI emission. Our method is particularly sensitive to short-period terrestrial planets, whose auroral power (if an atmosphere is present) is large and whose large RV will Doppler-shift the signal by one or more Å. Future high-resolution spectroscopy observations of our nearest neighbors could thus reveal the presence of unknown terrestrial exoplanets, including ones in the habitable zone.

All code used to generate the tables and figures in this paper is open source and available at <https://github.com/rodluger/exoaurora>.

We thank G. Anglada-Escude and the Pale Red Dot team for making their data publicly available, Giada Arney for useful discussions, and Service (1907) for poetic inspiration. DPF is supported by an NSF IGERT DGE-1258485 fellowship. This work was supported by the NASA Astrobiology Institutes Virtual Planetary Laboratory under Cooperative Agreement number NNA13AA93A. This work was based on data products

from observations made with ESO Telescopes at the La Silla Paranal Observatory under programme IDs 072.C-0488(E), 082.C-0718(B), 096.C-0082(A), 096.C-0082(B), 096.C-0082(C), 096.C-0082(D), 096.C-0082(E), 096.C-0082(F), 183.C-0437(A), and 191.C-0505(A). This work made use of the advanced computational, storage, and networking infrastructure provided by the Hyak super-computer system at the University of Washington.

## REFERENCES

- Agol, E. 2007, *MNRAS*, 374, 1271
- Anglada-Escudé, G., Amado, P. J., Barnes, J., Berdiñas, Z. M., Butler, R. P., Coleman, G. A. L., de La Cueva, I., Dreizler, S., Endl, M., Giesers, B., Jeffers, S. V., Jenkins, J. S., Jones, H. R. A., Kiraga, M., Kürster, M., López-González, M. J., Marvin, C. J., Morales, N., Morin, J., Nelson, R. P., Ortiz, J. L., Ofir, A., Paardekooper, S.-J., Reiners, A., Rodríguez, E., Rodríguez-López, C., Sarmiento, L. F., Strachan, J. P., Tsapras, Y., Tuomi, M., & Zechmeister, M. 2016, *Nature*, 536, 437
- Barnes, R., Deitrick, R., Luger, R., Driscoll, P. E., Quinn, T. R., Fleming, D. P., Guyer, B., McDonald, D. V., Meadows, V. S., Arney, G., Crisp, D., Domagal-Goldman, S. D., Lincowski, A., Lustig-Yaeger, J., & Schwietermann, E. 2016, *ArXiv e-prints*
- Bastian, T. S., Dulk, G. A., & Leblanc, Y. 2000, *ApJ*, 545, 1058
- Berta-Thompson, Z. K., Irwin, J., Charbonneau, D., Newton, E. R., Dittmann, J. A., Astudillo-Defru, N., Bonfils, X., Gillon, M., Jehin, E., Stark, A. A., Stalder, B., Bouchy, F., Delfosse, X., Forveille, T., Lovis, C., Mayor, M., Neves, V., Pepe, F., Santos, N. C., Udry, S., & Wünsche, A. 2015, *Nature*, 527, 204
- Beuzit, J.-L., Feldt, M., Dohlen, K., Mouillet, D., Puget, P., Wildi, F., Abe, L., Antichi, J., Baruffolo, A., Baudoz, P., Boccaletti, A., Carbillet, M., Charton, J., Claudi, R., Downing, M., Fabron, C., Feautrier, P., Fedrigo, E., Fusco, T., Gach, J.-L., Gratton, R., Henning, T., Hubin, N., Joos, F., Kasper, M., Langlois, M., Lenzen, R., Moutou, C., Pavlov, A., Petit, C., Pragt, J., Rabou, P., Rigal, F., Roelfsema, R., Rousset, G., Saisse, M., Schmid, H.-M., Stadler, E., Thalmann, C., Turatto, M., Udry, S., Vakili, F., & Waters, R. 2008, in *Ground-based and Airborne Instrumentation for Astronomy II*, ed. I. S. McLean & M. M. Casali (SPIE-Intl Soc Optical Eng)
- Bhardwaj, A. & Gladstone, G. R. 2000, *Reviews of Geophysics*, 38, 295
- Broggi, M., de Kok, R. J., Birkby, J. L., Schwarz, H., & Snellen, I. A. G. 2014, *A&A*, 565, A124
- Broggi, M., Snellen, I. A. G., de Kok, R. J., Albrecht, S., Birkby, J., & de Mooij, E. J. W. 2012, *Nature*, 486, 502
- Cabannes, J. & Dufay, J. 1955, *J. Phys. Radium*, 16, 129
- Chamberlain, J. W. 1961, *Physics of the aurora and airglow*
- Cheng, A. F. 1990, *Geophysical Research Letters*, 17, 1669
- Cohen, O., Drake, J. J., Gloer, A., Garraffo, C., Poppenhaeger, K., Bell, J. M., Ridley, A. J., & Gombosi, T. I. 2014, *ApJ*, 790, 57
- Connerney, J. E. P., Acua, M. H., & Ness, N. F. 1991, *Journal of Geophysical Research: Space Physics*, 96, 19023
- Cowan, N. B., Agol, E., & Charbonneau, D. 2007, *MNRAS*, 379, 641
- Crossfield, I. J. M., Hansen, B. M. S., Harrington, J., Cho, J. Y.-K., Deming, D., Menou, K., & Seager, S. 2010, *ApJ*, 723, 1436
- Dalcanton, J., Seager, S., Aigrain, S., Battel, S., Brandt, N., Conroy, C., Feinberg, L., Gezari, S., Guyon, O., Harris, W., Hirata, C., Mather, J., Postman, M., Redding, D., Schiminovich, D., Stahl, H. P., & Tumlinson, J. 2015, *ArXiv e-prints*
- Davenport, J. R. A., Kipping, D. M., Sasselov, D., Matthews, J. M., & Cameron, C. 2016, *ArXiv e-prints*
- Delchambre, L. 2015, *MNRAS*, 446, 3545
- Dempsey, J. T., Storey, J. W. V., & Phillips, A. 2005, *PASA*, 22, 91
- Dou, J.-P., Ren, D.-Q., & Zhu, Y.-T. 2010, *Research in Astronomy and Astrophysics*, 10, 189
- Driscoll, P. & Olson, P. 2011, *Icarus*, 213, 12
- Faigler, S. & Mazeh, T. 2011, *MNRAS*, 415, 3921
- Gillon, M., Jehin, E., Lederer, S. M., Delrez, L., de Wit, J., Burdanov, A., Van Grootel, V., Burgasser, A. J., Triaud, A. H. M. J., Opitom, C., Demory, B.-O., Sahu, D. K., Bardalez Gagliuffi, D., Magain, P., & Queloz, D. 2016, *Nature*, 533, 221
- Gonzalez, W., Joselyn, J., Kamide, Y., Kroehl, H., Rostoker, G., Tsurutani, B., & Vasyliunas, V. 1994, *Journal of Geophysical Research: Space Physics*, 99, 5771
- Gonzalez, W. D., Tsurutani, B. T., & De Gonzalez, A. L. C. 1999, *Space Science Reviews*, 88, 529
- Gopalswamy, N., Yashiro, S., Michalek, G., Stenborg, G., Vourlidas, A., Freeland, S., & Howard, R. 2009, *Earth, Moon, and Planets*, 104, 295
- Gray, C. L., Chanover, N. J., Slinger, T. G., & Molaverdikhani, K. 2014, *Icarus*, 233, 342
- Grießmeier, J.-M., Zarka, P., & Spreuw, H. 2007, *A&A*, 475, 359
- Guyon, O., Martinache, F., Cady, E. J., Belikov, R., Balasubramanian, K., Wilson, D., Clergeon, C. S., & Mateen, M. 2012, *How ELTs will acquire the first spectra of rocky habitable planets*
- He, M. Y., Triaud, A. H. M. J., & Gillon, M. 2016, *ArXiv e-prints*
- Hess, S. L. G. & Zarka, P. 2011, *A&A*, 531, A29
- Hubert, B., Grard, J.-C., Evans, D. S., Meurant, M., Mende, S. B., Frey, H. U., & Immel, T. J. 2002, *Journal of Geophysical Research: Space Physics*, 107, SMP 15
- Hunten, D. M., Rundle, H. N., Shepherd, G. G., & Vallance Jones, A. 1967, *Appl. Opt.*, 6, 1609
- Johns, M., McCarthy, P., Raybould, K., Bouchez, A., Farahani, A., Filgueira, J., Jacoby, G., Shectman, S., & Sheehan, M. 2012, in *Proc. SPIE*, Vol. 8444, *Ground-based and Airborne Telescopes IV*, 84441H
- Kawahara, H., Murakami, N., Matsuo, T., & Kotani, T. 2014, *ApJS*, 212, 27
- Khodachenko, M. L., Ribas, I., Lammer, H., Grießmeier, J.-M., Leitner, M., Selsis, F., Eiroa, C., Hanslmeier, A., Biernat, H. K., Farrugia, C. J., et al. 2007, *Astrobiology*, 7, 167
- Kivelson, M. G. & Russell, C. T. 1995, *Introduction to Space Physics*, 586
- Knutson, H. A., Charbonneau, D., Allen, L. E., Burrows, A., & Megeath, S. T. 2008, *ApJ*, 673, 526
- Knutson, H. A., Charbonneau, D., Allen, L. E., Fortney, J. J., Agol, E., Cowan, N. B., Showman, A. P., Cooper, C. S., & Megeath, S. T. 2007, *Nature*, 447, 183
- Kouveliotou, C., Agol, E., Batalha, N., Bean, J., Bentz, M., Cornish, N., Dressler, A., Figueroa-Feliciano, E., Gaudi, S., Guyon, O., Hartmann, D., Kalirai, J., Niemann, M., Ozel, F., Reynolds, C., Roberge, A., Straughn, K. S. A., Weinberg, D., & Zmuidzinas, J. 2014, *ArXiv e-prints*
- Kreidberg, L. & Loeb, A. 2016, *ArXiv e-prints*
- Lovis, C., Snellen, I., Mouillet, D., Pepe, F., Wildi, F., Astudillo-Defru, N., Beuzit, J.-L., Bonfils, X., Cheetham, A., Conod, U., Delfosse, X., Ehrenreich, D., Figueira, P., Forveille, T., Martins, J. H. C., Quanz, S., Santos, N. C., Schmid, H.-M., Ségransan, D., & Udry, S. 2016, *ArXiv e-prints*
- Luger, R. & Barnes, R. 2015, *Astrobiology*, 15, 119

- Macintosh, B., Graham, J. R., Ingraham, P., Konopacky, Q., Marois, C., Perrin, M., Poyneer, L., Bauman, B., Barman, T., Burrows, A. S., Cardwell, A., Chilcote, J., Rosa, R. J. D., Dillon, D., Doyon, R., Dunn, J., Erikson, D., Fitzgerald, M. P., Gavel, D., Goodsell, S., Hartung, M., Hibon, P., Kalas, P., Larkin, J., Maire, J., Marchis, F., Marley, M. S., McBride, J., Millar-Blanchaer, M., Morzinski, K., Norton, A., Oppenheimer, B. R., Palmer, D., Patience, J., Pueyo, L., Rantakyro, F., Sadakuni, N., Saddlemyer, L., Savransky, D., Serio, A., Soummer, R., Sivaramakrishnan, A., Song, I., Thomas, S., Wallace, J. K., Wiktorowicz, S., & Wolff, S. 2014, *Proceedings of the National Academy of Sciences*, 111, 12661
- Mauk, B. & Bagenal, F. 2012, Washington DC American Geophysical Union Geophysical Monograph Series, 197
- Mauk, B. H., Krimigis, S. M., & Acua, M. H. 1994, *Journal of Geophysical Research: Space Physics*, 99, 14781
- Maurin, A. S., Selsis, F., Hersant, F., & Belu, A. 2012, *A&A*, 538, A95
- Mazin, B. A., Bumble, B., Meeker, S. R., O'Brien, K., McHugh, S., & Langman, E. 2012, *Optics Express*, 20, 1503
- Mazin, B. A., Meeker, S., Strader, M., Szypryt, P., Walter, A., Bockstiegel, C., Collura, G., Mawet, D., Jensen-Clem, R., Guyon, O., Jovanovic, N., Oppenheimer, R., & Serabyn, E. 2015, in *AAS/Division for Extreme Solar Systems Abstracts*, Vol. 3, *AAS/Division for Extreme Solar Systems Abstracts*, 104.07
- Meadows, V. S., Arney, G. N., Schwieterman, E. W., Lustig-Yaeger, J., Lincowski, A. P., Robinson, T., Domagal-Goldman, S. D., Barnes, R. K., Fleming, D. P., Deitrick, R., Luger, R., Driscoll, P. E., Quinn, T. R., & Crisp, D. 2016, *ArXiv e-prints*
- Mennesson, B., Gaudi, S., Seager, S., Cahoy, K., Domagal-Goldman, S., Feinberg, L., Guyon, O., Kasdin, J., Marois, C., Mawet, D., Tamura, M., Mouillet, D., Prusti, T., Quirrenbach, A., Robinson, T., Rogers, L., Scowen, P., Somerville, R., Stapelfeldt, K., Stern, D., Still, M., Turnbull, M., Booth, J., Kiessling, A., Kuan, G., & Warfield, K. 2016, *The Habitable Exoplanet (HabEx) Imaging Mission: preliminary science drivers and technical requirements*
- O'Malley-James, J. T. & Kaltenegger, L. 2016, *ArXiv e-prints*
- Parker, E. N. 1958, *The Astrophysical Journal*, 128, 664
- Preusse, S., Kopp, A., Büchner, J., & Motschmann, U. 2007, *Planetary and Space Science*, 55, 589
- Reiners, A. & Basri, G. 2008, *A&A*, 489, L45
- Riaud, P. & Schneider, J. 2007, *A&A*, 469, 355
- Ribas, I., Bolmont, E., Selsis, F., Reiners, A., Lecointe, J., Raymond, S. N., Engle, S. G., Guinan, E. F., Morin, J., Turbet, M., Forget, F., & Anglada-Escudé, G. 2016, *ArXiv e-prints*
- Rimmer, P. B., Helling, C., Morley, C., Littlefair, S., & Hallinan, G. 2015, in *AAS/Division for Extreme Solar Systems Abstracts*, Vol. 3, *AAS/Division for Extreme Solar Systems Abstracts*, 104.15
- Robinson, T. D., Stapelfeldt, K. R., & Marley, M. S. 2016, *PASP*, 128, 025003
- Sandel, B. R., Herbert, F., Dessler, A. J., & Hill, T. W. 1990, *Geophysical Research Letters*, 17, 1693
- Schaefer, L., Wordsworth, R., Berta-Thompson, Z., & Sasselov, D. 2016, *ArXiv e-prints*
- Selsis, F., Wordsworth, R. D., & Forget, F. 2011, *A&A*, 532, A1
- Service, R. W. 1907, *The Cremation of Sam McGee in Songs of a Sourdough* (Toronto: W. Briggs)
- Seth, S., Haider, S., & Oyama, K. 2002, *Journal of Geophysical Research: Space Physics*, 107
- Skidmore, W., TMT International Science Development Teams, & Science Advisory Committee, T. 2015, *Research in Astronomy and Astrophysics*, 15, 1945
- Slanger, T. G., Cosby, P. C., Huestis, D. L., & Bida, T. A. 2001, *Science*, 291, 463
- Smith, D. S., Scalo, J., & Wheeler, J. C. 2004, *Icarus*, 171, 229
- Snellen, I., de Kok, R., Birkby, J. L., Brandl, B., Brogi, M., Keller, C., Kenworthy, M., Schwarz, H., & Stuik, R. 2015, *A&A*, 576, A59
- Sparks, W. B. & Ford, H. C. 2002, *ApJ*, 578, 543
- Steele, D. P. & McEwen, D. J. 1990, *Journal of Geophysical Research: Space Physics*, 95, 10321
- Stevenson, K. B., Désert, J.-M., Line, M. R., Bean, J. L., Fortney, J. J., Showman, A. P., Kataria, T., Kreidberg, L., McCullough, P. R., Henry, G. W., Charbonneau, D., Burrows, A., Seager, S., Madhusudhan, N., Williamson, M. H., & Homeier, D. 2014, *Science*, 346, 838
- Strickland, D. J., Hecht, J. H., Christensen, A. B., & McEwen, D. J. 2000, *Journal of Geophysical Research: Space Physics*, 105, 2461
- Turbet, M., Lecointe, J., Selsis, F., Bolmont, E., Forget, F., Ribas, I., Raymond, S. N., & Anglada-Escudé, G. 2016, *ArXiv e-prints*
- Udry, S., Lovis, C., Bouchy, F., Collier Cameron, A., Henning, T., Mayor, M., Pepe, F., Piskunov, N., Pollacco, D., Queloz, D., Quirrenbach, A., Rauer, H., Rebolo, R., Santos, N. C., Snellen, I., & Zerbi, F. 2014, *ArXiv e-prints*
- Vasyliunas, V. M., Kan, J. R., Siscoe, G. L., & Akasofu, S.-I. 1982, *Planetary and Space Science*, 30, 359
- Wang, C., Han, J. P., Li, H., Peng, Z., & Richardson, J. D. 2014, *Journal of Geophysical Research: Space Physics*, 119, 6199
- Wark, D. Q. 1960, *ApJ*, 131, 491
- West, A. A., Hawley, S. L., Bochanski, J. J., Covey, K. R., Reid, I. N., Dhital, S., Hilton, E. J., & Masuda, M. 2008, *AJ*, 135, 785
- Wood, B., Müller, H.-R., Zank, G., Izmodenov, V., & Linsky, J. 2004, *Advances in Space Research*, 34, 66
- Wood, B. E., Müller, H.-R., Zank, G. P., Linsky, J. L., & Redfield, S. 2005, *The Astrophysical Journal Letters*, 628, L143
- Zarka, P. 2007, *Planet. Space Sci.*, 55, 598
- Zellem, R. T., Lewis, N. K., Knutson, H. A., Griffith, C. A., Showman, A. P., Fortney, J. J., Cowan, N. B., Agol, E., Burrows, A., Charbonneau, D., Deming, D., Laughlin, G., & Langton, J. 2014, *ApJ*, 790, 53
- Zuluaga, J. I. & Bustamante, S. 2016, *ArXiv e-prints*